Plasma Science and Technology

PAPER

On the evolution and formation of discharge morphology in pulsed dielectric barrier discharge

To cite this article: Xingyu CHEN *et al* 2024 *Plasma Sci. Technol.* **26** 045403

Plasma Sci. Technol. **26** (2024) 045403 (13pp) https://doi.org/10.1088/2058-6272/ad13e4

On the evolution and formation of discharge morphology in pulsed dielectric barrier discharge

Xingyu CHEN (陈星宇)[1], **Mengqi LI** (李孟琦)[1], **Weiyi WANG** (王威逸)[1], **Quanzhi ZHANG** (张权治)[2], **Tao PENG** (彭涛)[3] **and Zilan XIONG** (熊紫兰)[1,*]

[1] State Key Laboratory of Advanced Electromagnetic Technology, Huazhong University of Science and Technology, Wuhan 430074, People's Republic of China
[2] School of Physics, Dalian University of Technology, Dalian 116024, People's Republic of China
[3] Wuhan National High Magnetic Field Center, Huazhong University of Science and Technology, Wuhan 430074, People's Republic of China

[*]E-mail of corresponding author: zilanxiong@hust.edu.cn

Received 4 September 2023, revised 7 December 2023
Accepted for publication 8 December 2023
Published 8 April 2024

Abstract

The discharge morphology of pulsed dielectric barrier discharge (PDBD) plays important roles in its applications. Here, we systematically investigated the effects of the voltage amplitude, discharge gap, and O_2 content on the PDBD morphology, and revealed the possible underlying mechanism of the U-shaped formation. First, the morphological evolution under different conditions was recorded. A unique U-shaped region appears in the middle edge region when the gap is larger than 2 mm, while the entire discharge region remains columnar under a 2 mm gap in He PDBD. The width of the discharge and the U-shaped region increase with the increase in voltage, and decrease with the increase of the gap and O_2 content. To explain this phenomenon, a two-dimensional symmetric model was developed to simulate the spatiotemporal evolution of different species and calculate the electric thrust. The discharge morphology evolution directly corresponds to the excited-state atomic reduction process. The electric thrust on the charged particles mainly determines the reaction region and strongly influences the U-shaped formation. When the gap is less than 2 mm, the electric thrust is homogeneous throughout the entire region, resulting in a columnar shape. However, when the gap is larger than 2 mm or O_2 is added, the electric thrust in the edge region becomes greater than that in the middle, leading to the U-shaped formation. Furthermore, in He PDBD, the charged particles generating electric thrust are mainly electrons and helium ions, while in He/O_2 PDBD those that generate electric thrust at the outer edge of the electrode surface are mainly various oxygen-containing ions.

Keywords: low-temperature plasma, dielectric barrier discharge, discharge morphology, particle distribution, electric thrust

(Some figures may appear in colour only in the online journal)

1. Introduction

Cold atmospheric pressure plasma (CAP) plays a vital role in many fields and is currently a prominent area of research in discharge plasma. The advancement of pulsed power technology has led to the emergence of pulsed dielectric barrier discharge (PDBD), which has found applications in medical sterilization, material modification, pollution control, agriculture, and the food industry [1–6]. In comparison to conventional AC DBD, PDBD can rapidly generate ionization waves with higher electron energy during ultra-fast rising and falling pulse edges. PDBD offers several advantages, including slight temperature increase during discharge, a wide range of chemical reactions, and various

* Author to whom any correspondence should be addressed.

active components [7–10]. Under specific conditions, it can produce large, uniform, and highly active non-equilibrium plasma, which has received increasing attention from researchers.

Numerous studies have emphasized the significance of the source configuration, charged particle density, type of active components, and spatial distribution of CAP in its practical applications [11, 12]. Understanding the evolution of plasma morphology and its formation mechanism is crucial for comprehending the physical processes of plasma, optimizing plasma treatment procedures, and enhancing the performance of plasma equipment. In the case of DBD, several investigations have explored the impact factors of different DBD morphologies under various driving power sources, DBD structures, and working gases [13–18]. Current studies demonstrate the close relationship between the morphological development and evolution of the discharge and microscopic factors such as the electric field distribution, particle species, and spatial distribution of the plasma [19–23]. However, the development and evolution of the morphology of PDBD and the related impact factors have been less explored.

Numerical simulations are also conducted to understand the influence of microscopic parameters of the DBD on the discharge morphology [24–26]. Li *et al* utilized a two-dimensional (2D) fluid model and discovered that the density of the positive ion cloud influenced the path and development speed of the jet streamer [27]. Qiao *et al* simulated the pattern evolution in a glow DBD system and found that the localized lateral electric field and its induced electron focusing effect are the controlling mechanism [28]. Marek *et al* revealed that the length of the surface streamlines along the dielectric surface was found to be voltage-dependent after a critical value of the charge density was reached [29]. Although the simulations helped to confirm and reveal the related factors in the development of plasma morphology, the underlying mechanism is not fully understood yet.

Current literature on the morphological changes of PDBD with parallel electrodes primarily focuses on the discharge mode transition and homogeneity [30, 31]. However, there is a strong need for more systematic research on the overall evolution of morphology and its formation mechanism [32]. In our previous study, we discovered that the 2D morphology distribution of PDBD significantly impacts the sterilization effect on a 2D membrane [33]. To further elucidate the evolution of the discharge morphology in PDBD, its formation mechanism, and the influencing factors, we systematically investigated the effects of parameters such as voltage amplitude, discharge gap, and O_2 content on the formation of the PDBD morphology through a combination of experiments and 2D numerical simulations. Initially, dynamic photos of the discharge process and static photos of the discharge morphology were captured using an intensified charge coupled device (ICCD) camera. The morphological evolution under different conditions was compared and analyzed. Subsequently, a 2D fluid model was developed, incorporating 34 selected particle reactions. This 2D model allowed us to obtain the 2D distributions of each charged particle and photon, as well as the electric thrust during the evolution process in the rising edge of the pulse. Finally, we analyzed the formation and development mechanism of the morphological features based on the obtained results.

2. Experimental setup and simulation

2.1. Experimental setup

A sketch of the experimental setup is shown in figure 1. The experimental platform primarily consists of a pulse generator (PVX4100), a high-voltage DC power supply (SL30PN300), a homemade DBD device, and various measurement instruments. The pulse generator and the high-voltage DC power supply were used to generate the high-voltage pulse signals. The applied voltage frequency was fixed at 8 kHz, and the pulse width at 2 μs, with rising and falling edges of 50 ns. To measure the electrical parameters, a high-voltage probe (Tektronix P6015A) and a current probe (Pearson P6585) were utilized. The discharge power was calculated through voltage–current integration. A high-speed camera ICCD (Andor DH712) was employed to record the static and dynamic discharge images. The gain of the microchannel plate (MCP) was 4095 and the gate width was 2 ns. The static discharge image is an accumulation of discharges during 80 periods (~0.01 s), while the dynamic image was recorded every 4 ns during the discharge period.

The DBD device comprises a pair of parallel electrodes mounted in the center of an acrylic cylindrical box. The copper electrode has a diameter of 25 mm and is covered with a threaded Teflon cylinder with a diameter of 45 mm for insulation. Dielectric sheets in the form of quartz plates with a diameter of 80 mm and a thickness of 1.2 mm were attached to the surface of the upper and lower electrodes. The distance between these quartz sheets, known as the gas gap, can be adjusted according to the requirements of the experiment. The working gas used in the experiments was either pure He or a mixture of He and O_2. The flow rate of the gas was maintained at a constant value of 0.5 L min^{-1}, controlled by a mass flow controller (MFC, D07-19B, 0-5 SLM). The ratios of O_2 in the mixture were adjusted between 1% and 12%.

2.2. Plasma simulation

COMSOL software was used to simulate the discharge process. A 2D symmetric model was employed, which closely resembled the structure of the device. Figure 2 shows a schematic diagram of the model, featuring a 6 mm gap. In the model, the electrode and dielectric sheet are represented as cylindrical, symmetrical structures. The dimensions of these structures in the model were set to match the actual values used in the experiment. The voltage at the high-voltage end was the same as in the experiment. A grid boundary layer was set at the interface of the quartz plate and gas to improve the accuracy of the calculation, and the complete grid contained 15220 domain cells and 696 boundary cells. Considering the periodicity of the discharge, the simulation

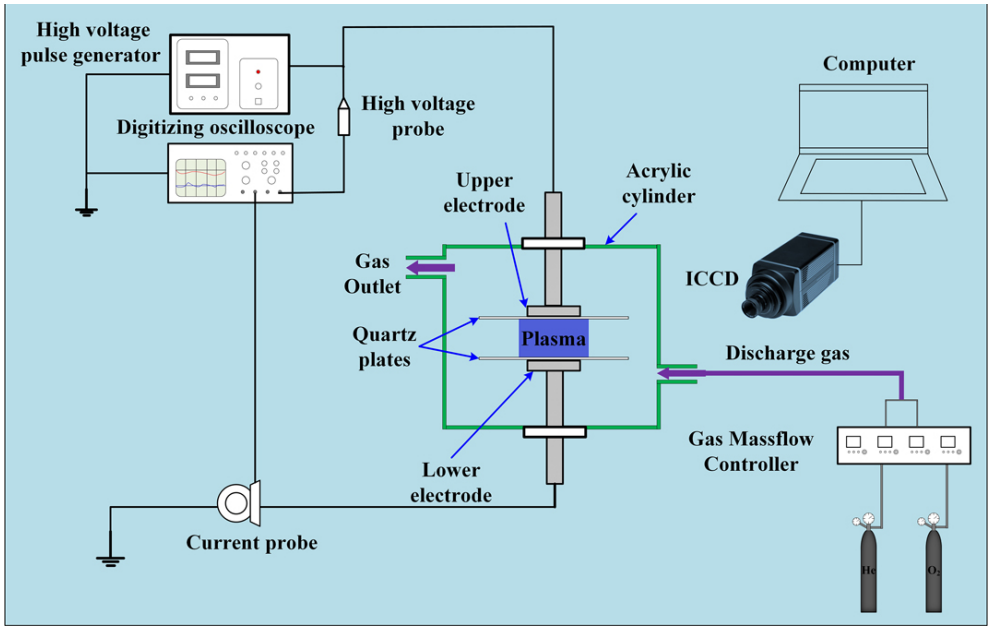

Figure 1. Sketch of the experimental setup.

time was 1 cycle (125 μs), and the time step of the simulation calculation was 1 ns.

The initial density of the electrons, n_{e0}, is 10^{13} m^{-3}, the initial velocity μ is 0. R_e is the source term of the rate and has an initial value of 0. The relationship between its concentration and time t satisfies the convective diffusion equation [34]:

$$\frac{\partial n_e}{\partial t} + \nabla \cdot \Gamma_e = R_e - (\mu \cdot \nabla) n_e, \tag{1}$$

where Γ_e is the electron density flux, which is used to obtain the spatial distribution of electron energy. The electron energy mobility and diffusivity are functions of the average electron energy calculated from the electron collision cross-section data. The solution equation is as follows:

$$\Gamma_e = -(\mu_e \cdot E) n_e - D_e \cdot \nabla n_e, \tag{2}$$

where μ_e is the electron mobility with an initial value of 0.1131 m^2 (V s)$^{-1}$. D_e characterizes the diffusive action term, which can be neglected concerning the drift term during the discharge. E is the electric field strength, which is calculated based on the Poisson equation:

$$E = -\nabla V. \tag{3}$$

The potential shift on the surface of the dielectric sheet satisfies the following equation:

$$D = \varepsilon E, \tag{4}$$

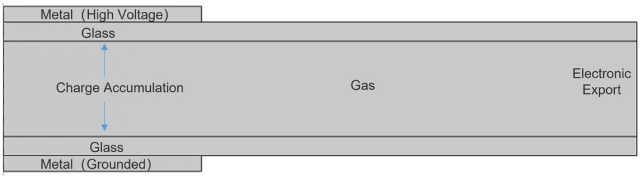

Figure 2. Schematic of the 2D symmetrical model.

where D denotes the potential shift and ε denotes the relative permittivity. The relative permittivity of air is 1, approximately the same as a vacuum. The relative permittivity of the dielectric sheet is 3.7.

The charge accumulated on the surface of the dielectric sheet satisfies the following equation:

$$-\boldsymbol{n} \cdot (D_1 - D_2) = \rho_s, \tag{5}$$

where $\boldsymbol{n}$ is the normal vector. D_1 and D_2 represent the potential shifts of quartz and gas.

The accumulation of charge and the surface current density satisfy the following equation:

$$\frac{\partial \rho_s}{\partial t} = \boldsymbol{n} \cdot \boldsymbol{J}_e + \boldsymbol{n} \cdot \boldsymbol{J}_i, \tag{6}$$

where $\boldsymbol{J}_i$ and $\boldsymbol{J}_e$ denote the ion and electron current density, respectively.

In order to consider the energy exchange during the discharge process, the energy conservation equation is introduced:

$$\frac{\partial n_\varepsilon}{\partial t} + \nabla \cdot \boldsymbol{j}_\varepsilon + \boldsymbol{E} \cdot \boldsymbol{j}_\varepsilon = S_\varepsilon, \tag{7}$$

where S_ε is the average net production rate of electron energies. $\boldsymbol{j}_\varepsilon$ is the flux density of electron energy, satisfying the following equation:

$$\boldsymbol{j}_\varepsilon = [-\nabla (D_e n_\varepsilon) + \mu_e n_\varepsilon V] \cdot 5/3, \tag{8}$$

n_ε is the average electron energy density, which satisfies the following equation:

$$n_\varepsilon = n_e \cdot (3k \cdot T_e / 2e). \tag{9}$$

Here, e represents the fundamental charge with a value of 1.6×10^{-19} C, and k represents the Boltzmann constant with a value of 1.38×10^{-23} J K^{-1}. T_e denotes the electron temperature. The plasma reactions involving He and O_2 consist of

numerous particles and reactions. The major particles considered in our simplified model are e, He^*, He^+, O, O_3, O^+, O_2^+, O^-, and O_2^-. The reactions involved and their corresponding rate coefficients are listed in table 1.

2.3. Electric thrust calculation

During the discharge process, the space-charged particles are accelerated by the electric field. When these particles collide with neutral gas molecules, new charged particles are ionized. These charged particles then move to the other electrode and out of the electrode area due to the force exerted by the electric field and other charged particles. This movement, known as electric thrust, causes the particles to diffuse, resulting in changes in the shape of the discharge. The electric thrust is the main factor responsible for the morphological changes [49]. In the presence of gas, the magnitude of the charged particle flow is a crucial physical parameter that characterizes the DBD thrust [50].

Using the fluid model, the thrust generated by each charged particle in the unit volume is obtained from the momentum theorem:

$$f_s = n_s m_s \nu_{sm} \mu_s, \tag{10}$$

where s presents the various charged particles, including e, the negative ions, and the positive ions. Only electrons and helium ions are included in pure He. The addition of O_2, O^+, O^-, O_2^+, and O_2^- also needs to be considered. n_s denotes the number of charged ions per unit volume, m_s denotes the mass of differently charged particles, ν_{sm} denotes the molecular momentum transfer frequency of different charged particles with neutral gas molecules, and μ_s denotes the average velocity of differently charged particles.

The current density equation is

$$J_s = e n_s \mu_s. \tag{11}$$

The drift velocity equation is

$$\mu_s = \frac{e}{m_s \nu_{sm}}. \tag{12}$$

From equations (4)–(6) and equations (10)–(12), the electric thrust can be calculated as follows:

$$f = e|n_i - n_n - n_e|E. \tag{13}$$

The electric thrust on the particle is proportional to the electric field strength E and the net charge.

3. Results and discussion

3.1. Effect of voltage amplitude, discharge gap, and O_2 content on the discharge morphology of PDBD

The waveforms of the applied voltage and the total current of a pulse period under a 6 mm gap at 8 kV in He PDBD are presented in figure 3(a). Two typical current pulses are observed at the rising and falling edges of the voltage pulse, similar to those reported in other literature [51]. The total current (I_t), displacement current (I_D), and discharge current (I_d) at the rising edge are presented in figure 3(b), and I_d is the difference between I_t and I_D. Figures 3(c) and (d) give the discharge currents under different O_2 contents at the rising and falling edges, respectively. The peak amplitude of the current at the rising edge is found to be larger than that at the falling edge with a fixed pulsed width of 2 μs, which may be

Table 1. Chemical reaction equations involved in He and He/O_2 discharge [35–48].

Reaction equation	Rate coefficient ($cm^3\ s^{-1}$)
$e + He \rightarrow He^* + e$	$4.2\times10^{-9}T_e^{0.31}e^{(-19.8/T_e)}$
$e + He^* \rightarrow He + e$	2.9×10^{-9}
$e + He \rightarrow He^+ + 2e$	$1.5\times10^{-9}T_e^{0.68}e^{(-24.6/T_e)}$
$e + He^* \rightarrow He^+ + 2e$	$1.28\times10^{-7}T_e^{0.6}e^{(-4.78/T_e)}$
$e + He^* \rightarrow He^+ + 2e$	2.7×10^{-10}
$He^* + He^* \rightarrow He^+ + e + He$	$1.327\times10^{-21}n_e(T_e/T_g)^{-0.44}$
$e + He^+ \rightarrow He$	$9.54\times10^{-12}T_e^{-1.05}e^{(-55.6/T_e)}$
$e + O_2 \rightarrow O_2^+ + 2e$	$8.8\times10^{-11}e^{(-4.4/T_e)}$
$e + O_2 \rightarrow O^- + O$	$2.2\times10^{-8}T_e^{-0.5}$
$e + O_2^+ \rightarrow O + O$	$2.0\times10^{-7}e^{(-5.5/T_e)}$
$e + O^- \rightarrow O + 2e$	$7.1\times10^{-12}T_e^{-1.05}e^{(-17/T_e)}$
$e + O_2 \rightarrow O^+ + O^- + e$	$5.3\times10^{-10}T_e^{0.9}e^{(-20/T_e)}$
$e + O_2 \rightarrow O^+ + O + 2e$	$4.2\times10^{-9}e^{(-5.6/T_e)}$
$e + O_2 \rightarrow O + O + e$	1.0×10^{-9}
$e + O_3 \rightarrow O_2^- + O$	$9.3\times10^{-10}T_e^{-0.62}$
$e + O_3 \rightarrow O^- + O_2$	$1.0\times10^{-8}(300/T_g)^{0.5}$
$e + O_3 \rightarrow O + O_2 + e$	$9.0\times10^{-9}T_e^{0.7}e^{(-13.6/T_e)}$
$e + O \rightarrow O^+ + 2e$	5.0×10^{-15}
$O^- + O_2 \rightarrow O_3 + e$	1.0×10^{-7}
$O^- + O_2^+ \rightarrow 3O$	$2.0\times10^{-7}(200/T_e)^{0.5}$
$O^- + O_2^+ \rightarrow O + O_2$	$2.0\times10^{-7}(300/T_e)^{0.5}$
$O^- + O^+ \rightarrow 2O$	$2.0\times10^{-7}e^{(300/T_g)}$
$O^+ + O_2^- \rightarrow O + O_2$	$2.0\times10^{-7}e^{(300/T_g)}$
$O_2^+ + O_2^- \rightarrow 2O_2$	2.0×10^{-11}
$O + O_3 \rightarrow 2O_2$	$1.5\times10^{-11}e^{(2250/T_g)}$
$He + O_2 \rightarrow He + O_2^+ + e$	$1.27\times10^{-10}(300/T_g)^{-0.5}$
$He + O \rightarrow He + O^+ + e$	$1.98\times10^{-10}(300/T_g)^{-0.5}$
$He^+ + O^- \rightarrow He + O$	$2.0\times10^{-7}e^{(300/T_g)}$
$He^+ + O_2^- \rightarrow He + O_2$	$2.0\times10^{-7}e^{(300/T_g)}$
$He^+ + O_2 \rightarrow He + O_2^+$	$3.3\times10^{-11}e^{(300/T_g)}$
$He^+ + O_2 \rightarrow He + O + O^+$	$3.3\times10^{-11}e^{(300/T_g)}$
$He^+ + O \rightarrow He + O^+$	$5.0\times10^{-11}(300/T_g)^{-0.5}$
$He + O_3 \rightarrow O + O_2 + He$	2.28×10^{-26}
$He^* + O_2 \rightarrow He + O_2^+ + e$	$2.54\times10^{-11}(300/T_g)^{-0.5}$

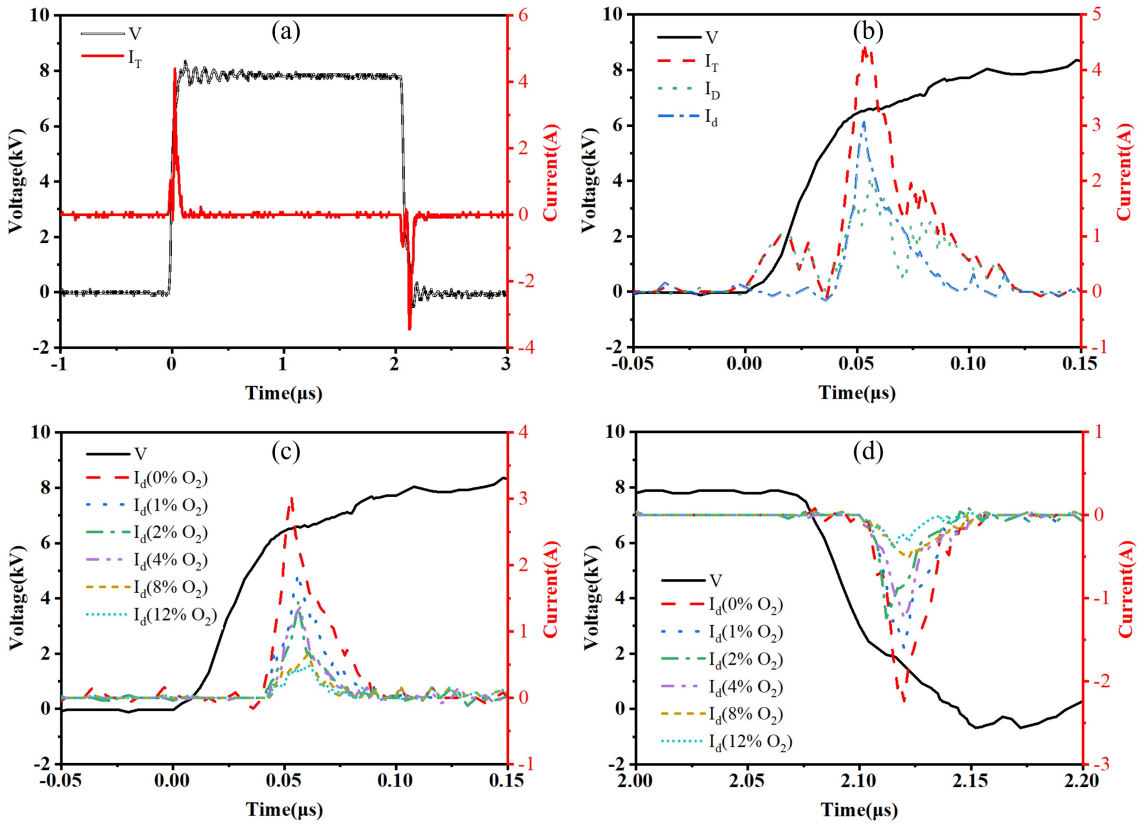

Figure 3. The measured voltage and current waveforms at 6 mm, 8 kV. (a) A whole pulse period, (b) I_t, I_D and I_d, (c) I_d under different O_2 contents at rising edge of the voltage pulse, (d) I_d under different O_2 contents at falling edge of the voltage pulse.

caused by the volume memory effects as illustrated in reference [51]. In addition, this difference is decreased with the increase in O_2 content. Meanwhile, both the current width and the peak amplitude at the rising and falling edge decrease with the increase in O_2 content.

Figure 4 presents the discharge power of the pure He and He/O_2 mixture PDBD under different discharge gaps and applied voltages. The discharge power basically increases with the applied voltage and decreases with the increase in the discharge gap and O_2 content. Under a 4 mm gap at 8 kV, the discharge power decreases from ~10 W to 1.5 W with 12% O_2 in the gas mixture, which is consistent with the trend of the discharge current.

Figure 5 presents static photos of the overall discharge morphology in pure He PDBD under different discharge gaps and applied voltages. The dashed lines in figure 3 indicate the area of the copper electrode and distinguish between the inside and outside of the electrodes. For a discharge gap of 2 mm, the discharge morphology appears columnar and gradually expands outward as the voltage increases. At 8 kV, the size of the morphology is approximately 50% larger than that of the electrode. When the discharge gap exceeds 2 mm, the discharge morphology becomes narrower in the middle and wider at the top and bottom edges. The width of the main discharge column area is smaller than the width of the copper electrode. Additionally, a U-shaped structure

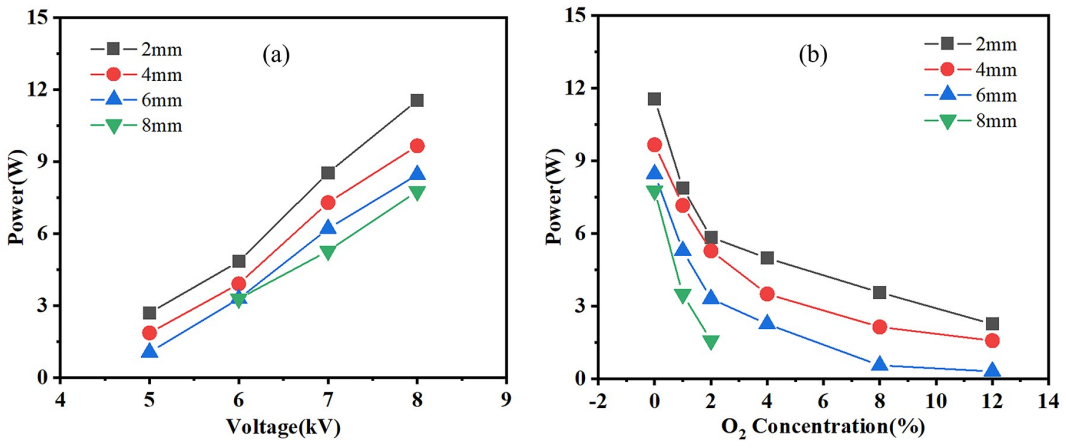

Figure 4. The discharge power of PDBD under different conditions. (a) Pure He and (b) He/O_2 mixture at 8 kV.

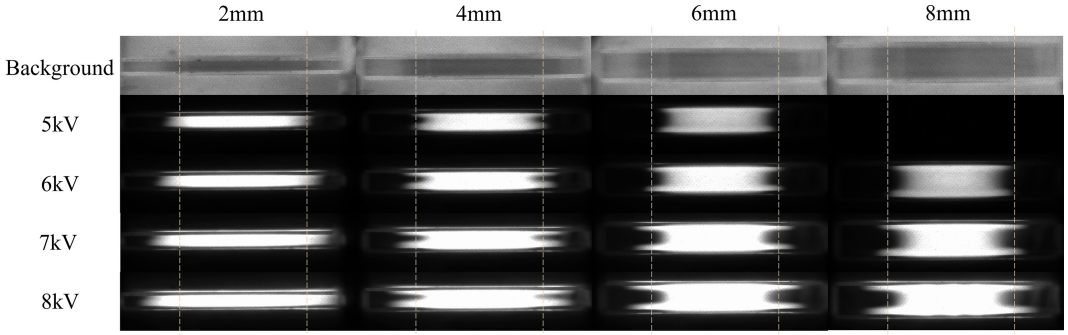

Figure 5. Photos of the discharge morphology variation with voltage amplitude and discharge gap in He PDBD. The photos are static photos taken by the ICCD camera.

emerges at the middle of the side edge, and its width increases with the increase in voltage amplitude. To further investigate the dimensions of the shape, the average of the diameters of the upper and lower edges of the discharge image was measured as the edge diameter, and the radius difference between the outer edge and the inner edge of the discharge was the width of the U-shaped structure. Figure 6 summarizes the width of the discharge morphology and the U-shaped structures in pure He under different discharge gaps and voltages.

Figure 7 shows static photos of the discharge morphology in He/O_2 mixture at various discharge gaps and O_2 content, at a fixed voltage of 8 kV. The images demonstrate that the diameter of the discharge area gradually decreases as the O_2 content increases. Additionally, the U-shaped structure appears under all conditions when O_2 is added to the working gas. The widths of the discharge region and the U-shaped structure decrease with the increase in O_2 content and discharge gap. At an O_2 content of 12%, the width of the discharge region becomes smaller than the diameter of the

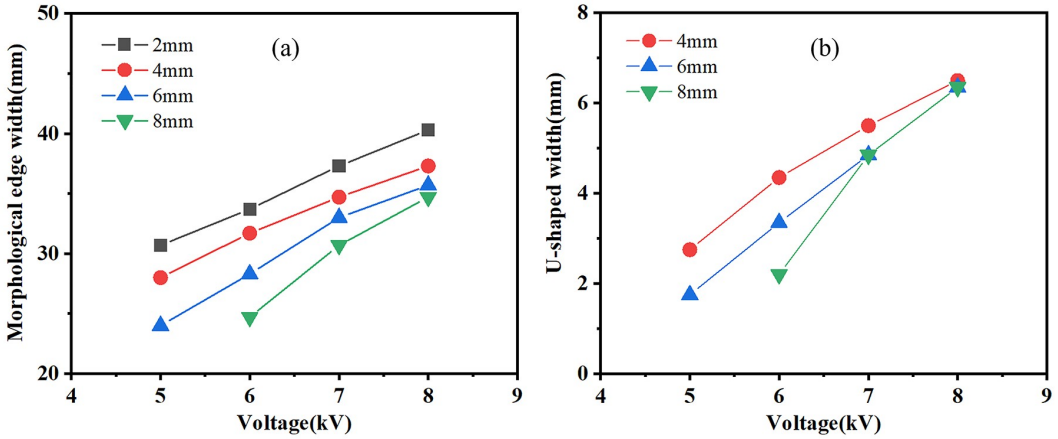

Figure 6. Size variation of PDBD morphology in He versus voltage amplitude and discharge gap. (a) Average width of the discharge region and (b) average width of the U-shaped structure.

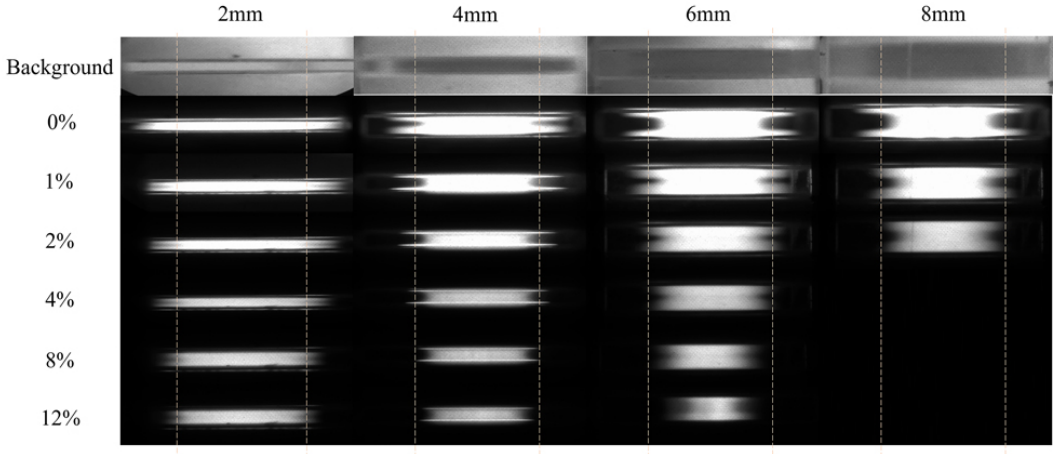

Figure 7. Photos of the discharge morphology variation with the discharge gap and O_2 content in He/O_2 PDBD. The photos are static photos taken by the ICCD camera.

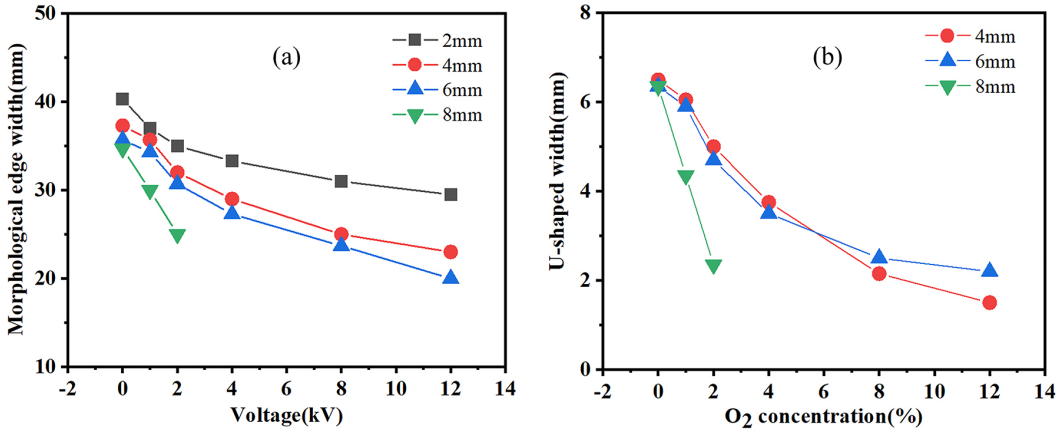

Figure 8. Size variation of PDBD morphology in He/O_2 versus O_2 content and discharge gap. (a) Width of the discharge region and (b) the average width of the U-shaped structures.

electrode for all discharge gaps. Figure 8 summarizes the widths of the discharge morphology and the U-shaped structures in He/O_2 discharges under different discharge gaps and O_2 contents.

3.2. Analysis of particle distribution and morphology evolution of PDBD in He

The morphology captured in the photographs provides a macroscopic representation of the photons produced when excited atoms undergo the reduction process. To examine the relationship between the morphology and the distribution of particles, we have chosen specific sets of experimental and simulation results for analysis. These sets include (1) pure helium with a 2 mm gap at 5 kV and 8 kV; (2) a 6 mm gap at 8 kV in helium with varying oxygen content of 1%, 2%, and 4%. It is important to note that the concentration of particles in different regions can differ significantly, sometimes by several orders of magnitude. Therefore, the density of each particle is represented logarithmically with a base of 10.

The dynamic development of PDBD was observed by capturing photos every 4 ns using an ICCD camera, and both the evolutions at the rising and falling edges of the voltage pulse were recorded. These photos allow us to study the evolution of the discharge morphology over time. Since we used a symmetrical pulse in the experiments, although the amplitude of the current pulse is slightly different in the rising and falling pulse edges due to the volume memory effects, the discharge morphology is almost the same (typical ICCD images of the discharge development at the falling edge are provided in the Appendix), so we only give the experimental and simulation results during the discharge at the rising edge here. Figure 9 presents the spatiotemporal morphology images and corresponding number densities of electrons, helium ions, and photons during the rising edge discharge at different discharge gaps and voltages in helium PDBD. Under a 2 mm discharge gap, as shown in figures 9 (a) and (b), the discharge morphology gradually expands from the middle area toward the outside of the electrode as the rising edge of the pulse develops. The overall discharge morphology appears columnar. The discharge intensity initially increases and then decreases during the rising edge discharge. With the increase in voltage, the field strength in the inner region of the electrode becomes larger, resulting in more energy being injected into the electrons. This leads to an increase in electron collision ionization and subsequently an increase in the electron density. For example, the maximum electron density under 5 kV is approximately 8×10^{15} m^{-3}, and the maximum electron density under 8 kV is around 5×10^{16} m^{-3}. These electron densities are generally consistent with those obtained by Pan *et al* under similar conditions [52]. Comparing the evolutions of particles at a fixed voltage of 8 kV under 2 mm and 6 mm discharge gaps, as shown in figures 9(b) and (c), the U-shaped structure gradually appears during the development of the rising edge discharge at around 60 ns under the 6 mm gap. The larger the discharge gap, the smaller the field strength in the inner region of the electrode, resulting in less energy being injected into the electrons and fewer electrons being produced through collision ionization. Consequently, the electron density decreases. At 72 ns, the electron density is approximately 5×10^{16} m^{-3} for the 2 mm gap, while it drops to around 7×10^{14} m^{-3} for the 6 mm gap, representing a decrease of nearly two orders of magnitude. Since helium ions are much heavier than electrons, their outward expansion is slower, and they remain confined within the electrode region.

The production of photons primarily occurs through the particle reaction $e + He^* \rightarrow He + e$. The number density of photons corresponds to the consumption of helium atoms in the excited state during this reaction. As time progresses, the region of photon aggregation continues to expand outward. The concentration of photons is positively correlated with the changes in discharge intensity spatio-temporally, and their distribution region aligns completely with the development of the discharge morphology. For instance, in the case of a 2 mm gap at 8 kV, the discharge area within the first 72 ns is primarily concentrated on the inner side of the electrode. During this period, the number density of photons gradually increases from 5×10^{12} m^{-3} at 8 ns to 1×10^{16} m^{-3} at 72 ns. After 72 ns, due to the outward expansion of electrons, electron collisions also occur on the top and bottom surfaces of

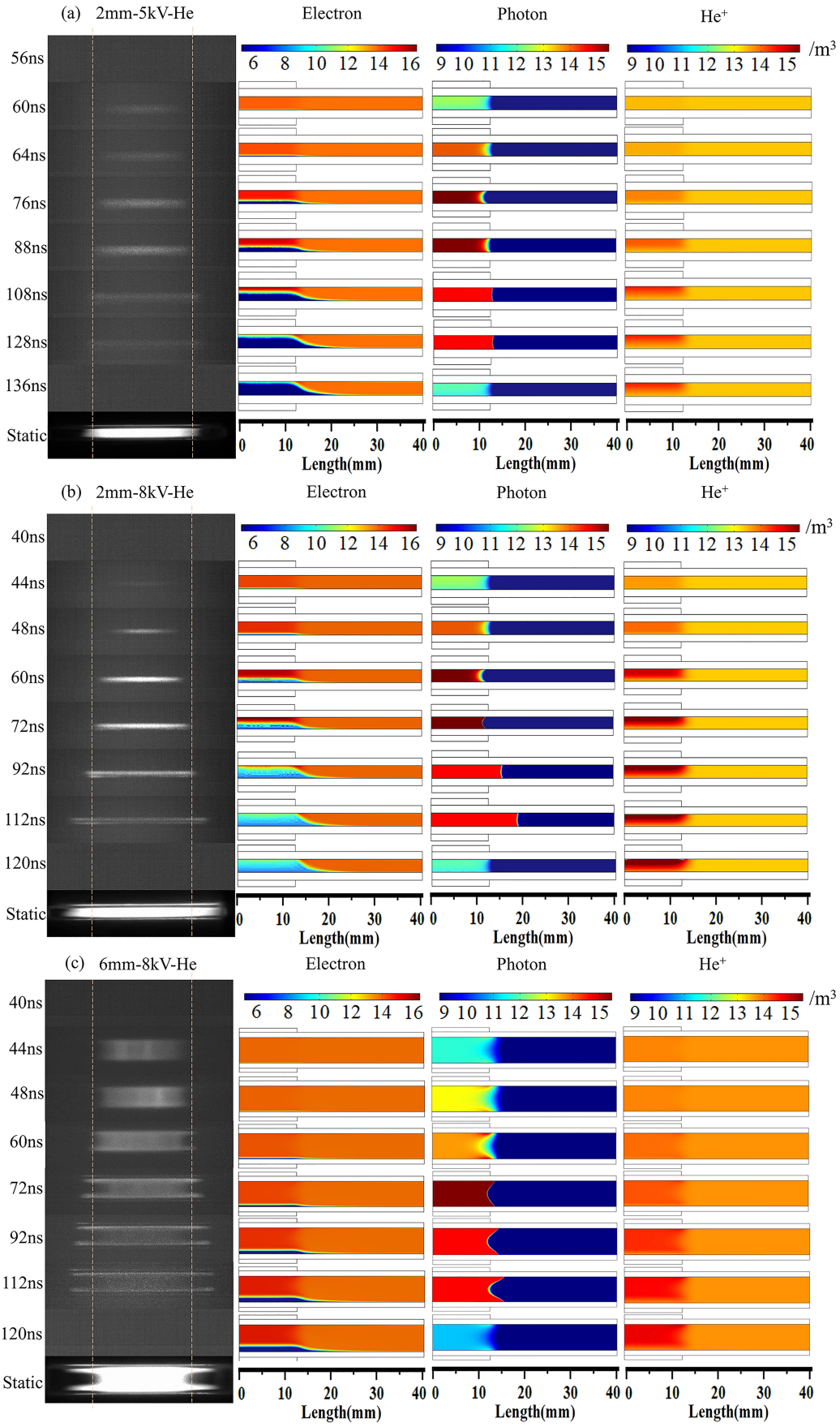

Figure 9. Evolution of the discharge morphology. Logarithm results of electron density, photon density, and helium ion density of the He PDBD during the voltage-rising edge period. (a) 2 mm, 5 kV, (b) 2 mm, 8 kV, (c) 6 mm, 8 kV.

the dielectric sheets. This leads to the production of excited-state helium atoms and photons outside the electrode area. However, at this stage, the density of photons produced decreases as the overall discharge weakens, reaching 6×10^{14} m^{-3} at 112 ns. It is worth noting that the photon number densities at the same time point for a 5 kV, 2 mm gap and an 8 kV, 6 mm gap are smaller compared to the 8 kV, 2 mm gap condition. This is due to the lower voltage and larger gap, which result in the reduced production of photons.

3.3. Analysis of particle distribution and morphology evolution of PDBD in He/O_2 mixture

Figure 10 illustrates the spatiotemporal morphology and the corresponding number densities of electrons, helium ions, photons, and oxygen-containing ions during the rising edge discharge under different O_2 contents in He/O_2 PDBD with a fixed discharge gap of 6 mm and voltage of 8 kV. The recorded luminous duration and the total discharge area decrease with the increase in O_2 content, and the electron number density decreases as the O_2 content increases,

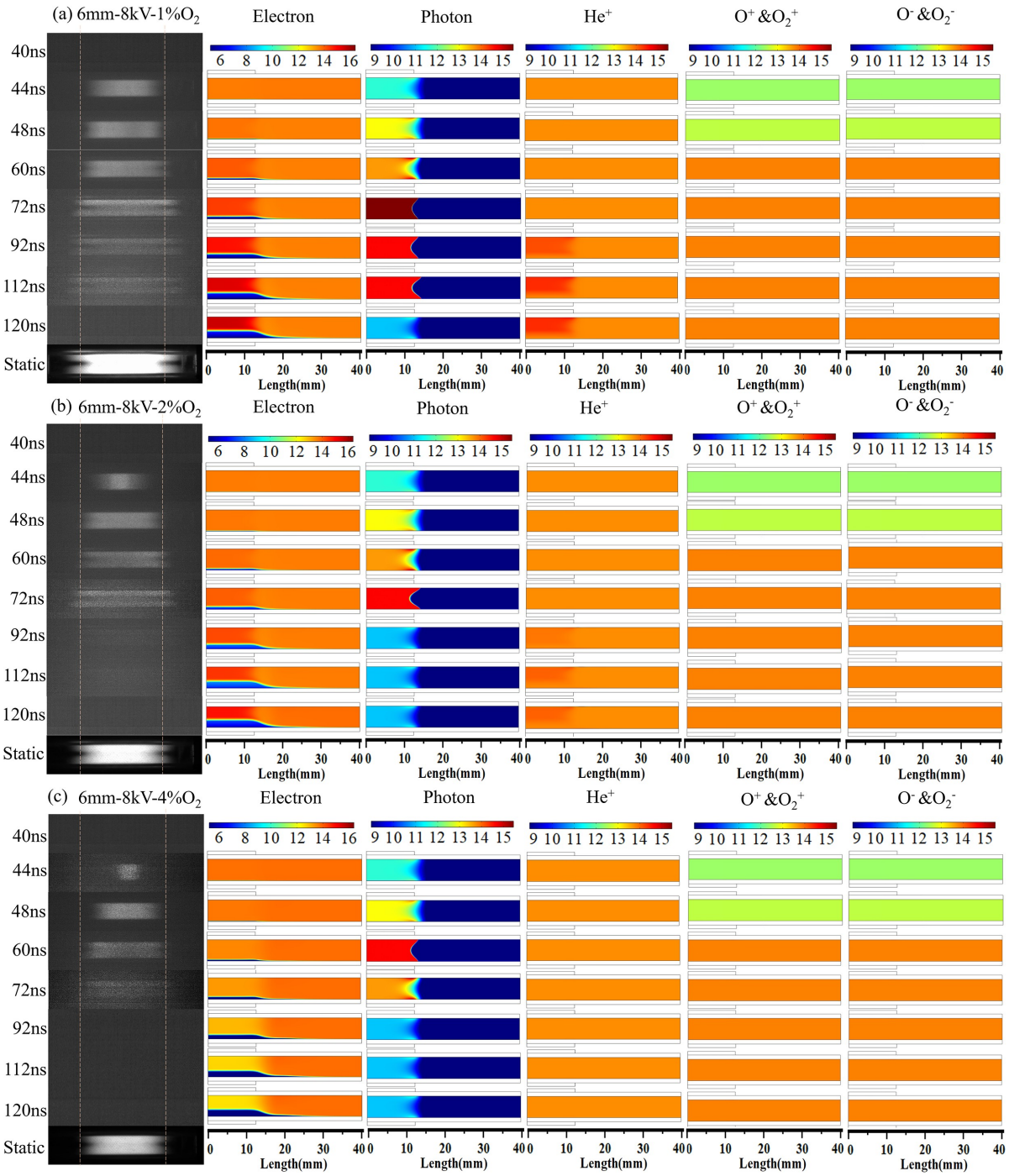

Figure 10. Evolution of the discharge morphology; logarithm results of electron density, photon density, helium ion density, and oxygen-containing ions of the He/O_2 PDBD at 8 kV, 6 mm gap during the voltage-rising edge period. (a) 1% O_2 content, (b) 2% O_2 content, (c) 4% O_2 content.

primarily due to the electronegativity of oxygen and the electron-oxygen collision reactions, which is consistent with the trend in discharge current in figure 3(c). The reduction of discharge duration and lower transferred charge and discharge power with the increasing O_2 concentration were also found in references [53, 54] under a N_2/O_2 filamentary DBD system observed by Höft *et al.* However, the trends of the discharge area and current peaks are opposite. These differences may be caused by the characteristics of the working gas, the discharge structure, and the discharge mode, which need systematic and comprehensive investigation in future work.

The density change of helium ions follows the same trend as electrons, resulting in a decrease in the number of helium atoms in excited states. Under 2% O_2 content, the electron number density is only 3.5×10^{14} m^{-3}. As the O_2 content continues to increase, the electron density within the electrode area becomes even lower than the initial value. After adding O_2, the photon aggregation zone keeps diffusing outward. However, due to the electronegativity of O_2 and the energy consumption involved in oxygen ionization reactions, the reduction reaction of excited-state helium atoms is significantly reduced. As a result, both the number density and the presence of photons decrease. Upon comparing the simulated results with the experimental results, it is observed that in all conditions, the trend of photon intensity and the spatial and temporal distribution of the aggregation zone align with the discharge intensity and the microscopic development process of discharge morphology.

During the He/O_2 discharge, electrons combine with oxygen to form various oxygen ions. The simulation results reveal the formation of two μm-level sheath layers consisting of positive and negative ions on the surfaces of the lower and upper dielectric plates, respectively. To investigate the impact of the sheath layer, the results under the condition of a 6 mm gap with 4% O_2 content at 72 ns are taken as an example. The overall number density distributions of O^+ & O_2^+ and O^- & O_2^- are shown in figures 11(a) and (b), respectively. For clearer comparison, the zoomed distribution results within 1 mm thickness around the negative and positive surfaces are presented in figures 11(c) and (d). The sheath layer has a width of approximately 27 mm, which is consistent with the width of the discharge morphology, and a thickness of around 100 μm. The number density of ions within the sheath layer is approximately 10^{15} m^{-3}, which is one order of magnitude higher than that of the surrounding region. Figures 11(e) and (f) display the distribution of helium ions and electrons within 1 mm thickness around the negative and positive surfaces, respectively. A similar sheath layer is observed, although the number density within the sheath region is smaller, approximately two orders of magnitude lower than those of the positive and negative oxygen ions.

3.4. Effect of electrical thrust on discharge morphology of PDBD

When the number of electrons in the avalanche head reaches

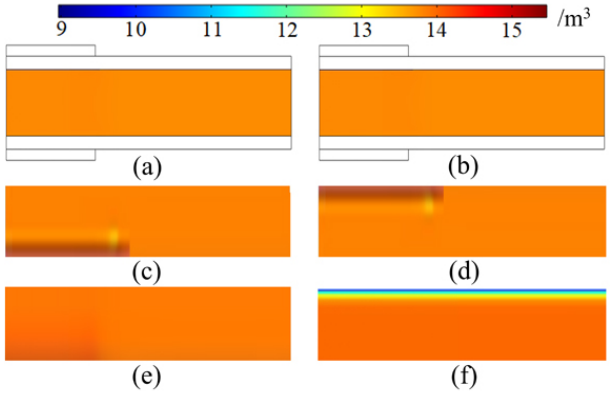

Figure 11. Logarithm results of the concentration distribution of charged particles in a 6 mm He/O_2 PDBD with 4% O_2 content at 72 ns. The overall distribution of (a) O^+ & O_2^+, (b) O^- & O_2^-, (c) O^+ & O_2^+ on negative sheath layer, (d) O^- & O_2^- on positive sheath layer, (e) helium ion on negative sheath layer, (f) electron on positive sheath layer.

a critical value N_{cr} (about 10^8), photoionization will play a dominant role, determined as $e^{\alpha d} \leqslant N_{cr}$ [55], where α is the ionization coefficient, d is the gas gap distance. In the corresponding electric field strength range in this paper, α can be approximately calculated by the following equation [56]:

$$\alpha = NAe^{-BN/E}, \tag{14}$$

where N is the gas molecular density, which is about 2.43×10^{25} m^{-3}, $A = 1.4\times10^{-20}$ m^2, and $B = 660$ Td (1 Td=10^{-21} V m^2). The calculations found that none of the values of $e^{\alpha d}$ found in this paper under the 2–8 mm gap exceeds 10^4, which is more than four orders lower than the critical value. That is, the discharge development in our situation is mainly dominated by collisional ionization, and the photoionization is negligible.

Based on the calculation formula for electric thrust, it is known that the electric thrust is directly proportional to the concentration difference between positive and negative charged particles and the electric field strength. By utilizing the known distribution of the concentration of each charged particle and the electric field, the distribution of electric thrust can be determined. Figure 12 illustrates the distribution of electric thrust under various conditions.

In pure He conditions, the primary charged particles consist of helium ions and electrons only. The helium ions are primarily confined to the inner side of the electrode due to their heavier mass. The electron density, on the other hand, plays a crucial role in determining the electric thrust on the outer side of the electrode. As shown in figures 12(a1) and (a2), for a 2 mm gap, the electron density is high in all regions. Electrons in the edge or middle region will be propelled outward by the electric thrust. This results in a significant concentration difference of charged particles in the outer region, both in the middle and at the edge. Consequently, both the middle region and the edge expand outward. At a voltage of 5 kV and 120 ns, the edge size is approximately 28 mm with a maximum electric thrust of around 9.5×10^{-4} N, while the maximum electric thrust in the

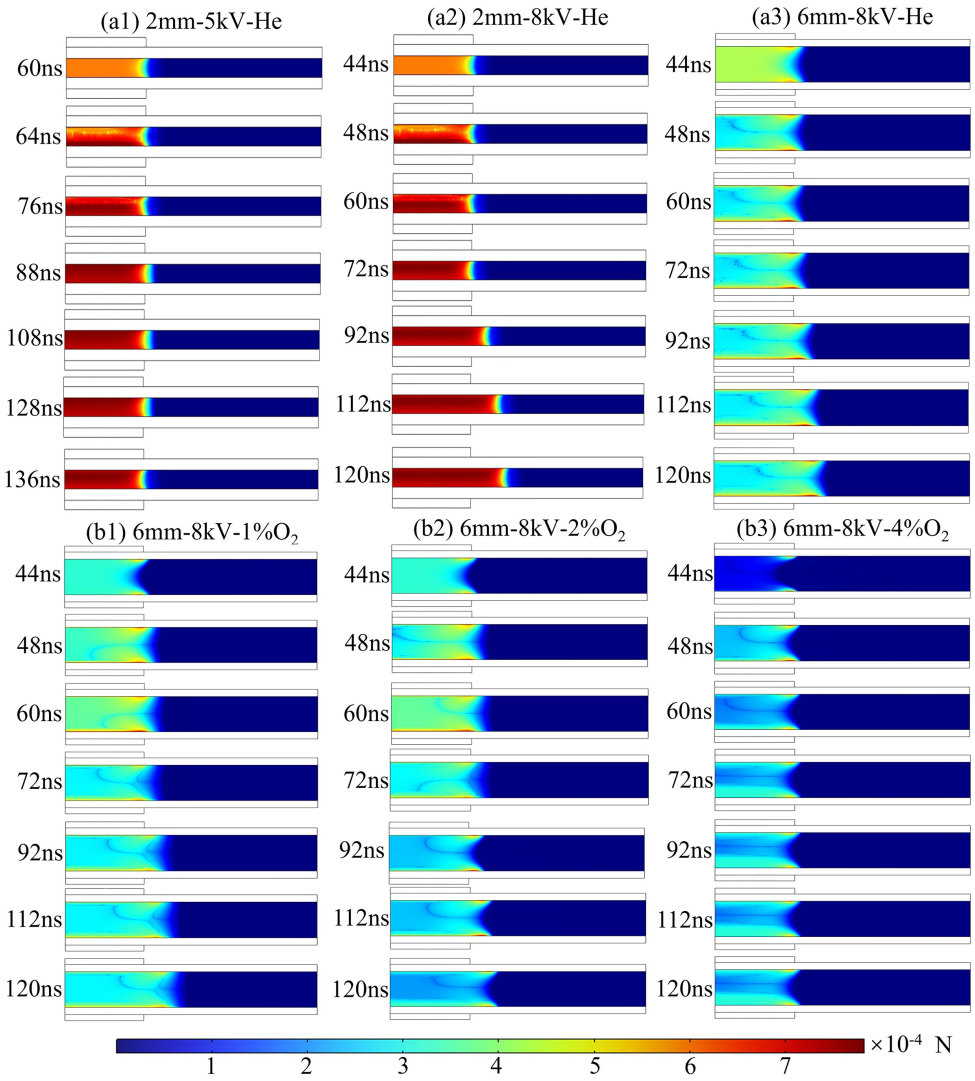

Figure 12. Electric thrust evolution process. (a1) 2 mm, 5 kV pure helium, (a2) 2 mm, 8 kV pure helium, (a3) 6 mm, 8 kV pure helium, (b1) 6 mm, 8 kV He/O_2 with 1% oxygen concentration, (b2) 6 mm, 8 kV He/O_2 with 2% oxygen concentration, (b3) 6 mm, 8 kV He/O_2 with 4% oxygen concentration.

middle region is approximately 8.7×10^{-4} N, slightly smaller than at the edge. At a voltage of 8 kV and 120 ns, the edge size increases to about 39 mm with a maximum electric thrust of approximately 9.7×10^{-4} N, and the maximum electric thrust in the middle region is around 9×10^{-4} N. In summary, in a He PDBD with a 2 mm gap, the maximum electric thrust at the edge and in the middle region is nearly the same at the same voltage, resulting in a columnar discharge morphology. As the voltage increases, the electric field on the outer side of the electrode strengthens, leading to a more powerful electric thrust and an increase in the size of the discharge.

The electric field strength, electron density, and electric thrust in each region under the remaining gaps are smaller compared to those at the 2 mm discharge gap at the same voltage level. In the He PDBD under the 6 mm gap (figure 12(a3)), the edge size measures 32 mm at 80 ns with a maximum electric thrust of approximately 7.6×10^{-4} N. On the other hand, the middle size is only 27 mm with a maximum electric thrust of around 3.9×10^{-4} N, which is only about half of the electric thrust observed in the edge area. The magnitude of the electric thrust calculated above is roughly similar to that reported by Elias *et al* [57]. The sheath layer at the edge will result in the formation of numerous charged particle aggregations. However, the electric thrust in the middle region is not sufficient to propel a large number of charged particles toward the outer side area of the electrodes. As a result, the discharge morphology takes on a distinct U-shape in the middle region.

For an 8 kV discharge with O_2 addition under a 6 mm gap, there are four additional charged particles present: O^+, O^-, O_2^+, and O_2^-, in addition to the helium ions and electrons. As depicted in figures 10, 11 and 12(b1)–(b3), it is evident that there is a significant variation in ion concentration only on the surface of the positive and negative dielectric plates, resulting in a noticeable electric thrust at the outer edge of the electrode. The difference in number density between electrons and helium ions in the sheath region is much

smaller compared to that of oxygen-containing ions. Therefore, the primary factor contributing to the electric thrust along the outer edge of the electrode surface is the oxygen-containing ions. However, increasing the O_2 content will weaken the motion of electrons and subsequently reduce the concentration of charged particles, leading to a decrease in electric thrust. For instance, the concentration of net negative ions at 4% O_2 content is only 70% of that observed under the same gap and voltage level in He PDBD. The edge size measures approximately 26.2 mm with a maximum electric thrust of around 5.4×10^{-4} N, while the middle size is approximately 20.8 mm with a maximum electric thrust of around 2.5×10^{-4} N. The electric thrust at the edge and in the middle is only 70% of that observed under the He PDBD condition.

The simulation results indicate that the formation of the PDBD morphology is strongly influenced by the movement of charged particles driven by the electric thrust. In the case of He PDBD, the charged particles that significantly impact the overall discharge morphology are electrons and helium ions. On the other hand, in He-O_2 PDBD, the charged particles that predominantly contribute to the development of the morphology at the outer edge of the electrodes are primarily oxygen-containing ions.

4. Conclusion

In this study, we conducted a systematic investigation into the development of discharge morphology and the possible mechanism of the U-shaped formation in PDBD. We performed experimental comparisons of morphological changes at different voltages, gas gaps, and O_2 content. The evolution of the discharge morphology was then compared with the trends observed in charged particles, excited state atoms, electric thrust, and other parameters using 2D simulations. Our findings revealed that the morphological changes in PDBD are closely correlated with the applied voltage, discharge gap, and gas composition. Under a 2 mm gap, the discharge exhibited a cylindrical shape in He PDBD. However, under larger gaps or with O_2 addition, a U-shaped structure began to appear at the middle edge of the discharge region. The width of the discharge and the U-shaped structure increased with the increase of the voltage amplitude and decreased with higher O_2 content.

The simulation results provided insights into the aggregation region and density of photons generated during the reduction of excited atoms, which were found to agree with the microscopic development of the discharge shape and intensity. Furthermore, the calculation of electric thrust demonstrated that it played a major role in driving the morphological changes. In He PDBD with a small 2 mm gap, the electric thrust in the middle region and at the outer edge of the electrodes was nearly identical, resulting in an overall column shape of the discharge region. However, as the discharge gap and O_2 content increased, the electric thrust in the middle region near the outer edge of the electrode became smaller compared to that along the outward electrode. This led to the formation of a U-shaped structure. In pure He PDBD, the formation of the discharge shape was primarily influenced by electrons and helium ions. In He/O_2 PDBD, the presence of oxygen-containing ions in the sheaths (O^+, O_2^+, O^-, and O_2^-) played a significant role in the formation of electric thrust along the outer side of the electrode.

Acknowledgments

The authors are grateful for financial support from the Interdisciplinary Fund of the Wuhan National High Magnetic Field Center (No. WHMFC202101).

Appendix

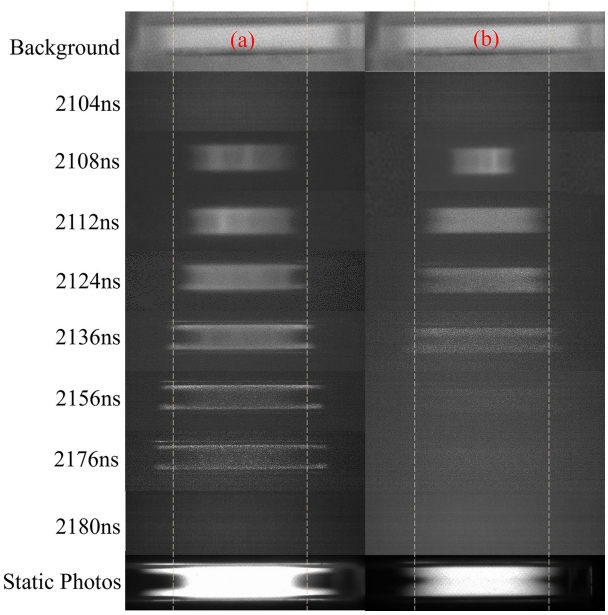

Figure A1. Evolution of the discharge morphology of the He PDBD during the falling edge period of the voltage pulse. (a) 6 mm, 8 kV, He, (b) 6 mm, 8 kV, 2% O_2.

References

[1] Hansen L *et al* 2021 *Plasma Sources Sci. Technol.* **30** 045004
[2] Bisag A *et al* 2020 *Plasma Process. Polym.* **17** 2000154
[3] Breden D, Miki K and Raja L L 2012 *Plasma Sources Sci. Technol.* **21** 034011
[4] Yusupov M *et al* 2023 *Plasma Process. Polym.* **20** 2200137
[5] Lu X, Laroussi M and Puech V 2012 *Plasma Sources Sci. Technol.* **21** 034005
[6] Cullen P J *et al* 2018 *Plasma Process. Polym.* **15** 1700085
[7] Iza F, Walsh J L and Kong M G 2009 *IEEE Trans. Plasma Sci.* **37** 1289
[8] Pai D Z *et al* 2009 *Plasma Sources Sci. Technol.* **18** 045030
[9] Huang B D *et al* 2015 *J. Phys. D: Appl. Phys.* **48** 125202
[10] Huang B D *et al* 2016 *J. Phys. D: Appl. Phys.* **49** 045202
[11] Moon S Y *et al* 2006 *Phys. Plasmas* **13** 033502

[12] Yao C W *et al* 2016 *IEEE Trans. Plasma Sci.* **44** 2576
[13] Wang Y Y *et al* 2021 *Plasma Sources Sci. Technol.* **30** 075009
[14] Liu F *et al* 2021 *J. Appl. Phys.* **129** 033302
[15] Lu X P and Ostrikov K 2018 *Appl. Phys. Rev.* **5** 031102
[16] Pinchuk M *et al* 2021 *Sci. Rep.* **11** 17286
[17] Li X C *et al* 2018 *IEEE Trans. Plasma Sci.* **46** 583
[18] Wu K Y *et al* 2020 *Phys. Plasmas* **27** 082308
[19] Zhou X Y *et al* 2021 *Plasma Sci. Technol.* **23** 064003
[20] Wang X L *et al* 2019 *IEEE Access* **7** 69748
[21] Wang Q *et al* 2019 *J. Phys. D: Appl. Phys.* **52** 205201
[22] Lieberman M A 2015 *Plasma Sources Sci. Technol.* **24** 025009
[23] Lazarou C *et al* 2015 *Plasma Sources Sci. Technol.* **24** 035012
[24] Seyfi P *et al* 2020 *J. Theor. Appl. Phys.* **14** 195
[25] Cai Y K, Lu L and Li P 2020 *Appl. Sci.* **10** 6766
[26] Wang Y G *et al* 2022 *Plasma Sources Sci. Technol.* **31** 105015
[27] Li X C *et al* 2022 *Phys. Fluids* **34** 027112
[28] Li B *et al* 2018 *J. Phys. D: Appl. Phys.* **51** 015203
[29] Florkowski M 2021 *Measurement* **186** 110170
[30] Bai Z G *et al* 2015 *J. Phys. D: Appl. Phys.* **48** 345201
[31] Ren C H *et al* 2022 *J. Phys. D: Appl. Phys.* **55** 235204
[32] Guo H F *et al* 2019 *J. Appl. Phys.* **125** 163304
[33] Chen X Y *et al* 2022 *Plasma Sci. Technol.* **24** 124015
[34] Sublet A *et al* 2006 *Plasma Sources Sci. Technol.* **15** 627
[35] Gudmundsson J T *et al* 2001 *J. Phys. D: Appl. Phys.* **34** 1100
[36] Tsang W and Hampson R F 1986 *J. Phys. Chem. Ref. Data* **15** 1087
[37] Demore W B *et al* 1985 *Int. J. Chem. Kinetics* **17** 1135
[38] Beall G H 1992 *Annu. Rev. Mater. Sci.* **22** 91
[39] Shi J C and Barker J R 1990 *Int. J. Chem. Kinetics* **22** 1283
[40] Atkinson R *et al* 1989 *J. Phys. Chem. Ref. Data* **18** 881
[41] Morgan J E, Phillips L F and Schiff H I 1962 *Discuss. Faraday Soc.* **33** 118
[42] Brauer I *et al* 1999 *J. Appl. Phys.* **85** 7569
[43] Borrell P *et al* 1985 *Ber. Bunsenges. Phys. Chem.* **89** 337
[44] Castellano E and Schumacher H J 1962 *Z. Phys. Chem.* **34** 198
[45] McCrumb J L and Kaufman F 1972 *J. Chem. Phys.* **57** 1270
[46] Léveillé V and Coulombe S 2005 *Plasma Sources Sci. Technol.* **14** 467
[47] Stafford D S and Kushner M J 2004 *J. Appl. Phys.* **96** 2451
[48] Atkinson R *et al* 1997 *J. Phys. Chem. Ref. Data* **26** 1329
[49] Enloe C L *et al* 2004 *AIAA J.* **42** 589
[50] Lee D *et al* 2005 *IEEE Trans. Plasma Sci.* **33** 949
[51] Höft H *et al* 2014 *J. Phys. D: Appl. Phys.* **47** 465206
[52] Pan G S *et al* 2016 *Phys. Plasmas* **23** 043508
[53] Höft H *et al* 2013 *J. Phys. D: Appl. Phys.* **46** 095202
[54] Höft H *et al* 2014 *J. Phys. D: Appl. Phys.* **47** 455202
[55] Dhali S K and Williams P F 1982 *J. Appl. Phys.* **62** 4696
[56] Sigmond R S 1984 *J. Appl. Phys.* **56** 1355
[57] Elias P Q and Castera P 2013 *J. Phys. D: Appl. Phys.* **46** 365204